

The benefits of structural disorder in natural cellular solids

D. Aranguren van Egmond^{1,*†}, B. Yu², S. Choukir³, S. Fu¹, C.V. Singh^{1,3}, G.D. Hibbard^{1,*},
B.D. Hatton^{1,3*}

¹Department of Materials Science and Engineering, University of Toronto, Toronto, Ontario, Canada M5S 3E4.

²Department of Materials Science and Engineering, McMaster University, Hamilton, Ontario, Canada L8S 4L7.

³Department of Mechanical and Industrial Engineering, University of Toronto, Toronto, Ontario, Canada M5S 3G8.

*Correspondence to: derek.aranguren@alum.utoronto.ca; benjamin.hatton@utoronto.ca;

†Present address: National Research Council of Canada, 100 Sussex Drive, Ottawa, Ontario, Canada K1A 0R6

Abstract: Architected cellular materials in nature such as trabecular bone and woods exhibit disordered porous structure that is neither fully random, nor perfectly ordered, and has not been systematically quantified before. We have used Voronoi cell patterning to quantify disorder for a range of biological and engineered cellular materials, using a ‘disorder parameter’ (δ). Ranges of disorder appear to be typical to certain plant, animal and fungi cellular materials. Using 3D printing and numerical methods, we demonstrate experimentally there is a range of ‘pseudo-order’ ($\delta=0.6 - 0.8$) which exhibits a >30% increase in fracture toughness (and equivalent strength) compared to fully-ordered, hexagonal honeycombs ($\delta=1.0$) of equal density. Our results suggest ‘tailored disorder’ as a new design paradigm for architected materials to improve damage tolerance, and an evolutionary advantage for the pseudo-order of biological cellular materials.

Keywords: disorder, bioinspiration, architected materials, cellular solids, damage tolerance, toughening mechanisms, 3D printing, additive manufacturing, mechanics

Porous, biological cellular materials such as wood (plant ground tissue), trabecular bone, corals, diatoms, and dentin combine complex biological functions with structural roles, such as skeletal support and impact protection (1, 2). Biological cellular materials typically feature highly complex structural hierarchies, from nano- to macroscale that enable optimization of both strength and toughness (flaw tolerance) simultaneously (3-9). The hierarchy of bone, for example, ranges over 9-10 orders of magnitude in length scale, from the molecular level to the macroscale (10, 11). Recently, there is great interest in the optimization of internally ‘architected’ engineering materials, featuring design across several length scales. Architected materials, be they biological or engineered, feature mechanical properties defined by composition and multiscale hierarchical geometry (3).

As illustrated in a cross-section view of a whale vertebra (trabecular bone) (**Fig 1a**), biological cellular materials are generally disordered in the spatial distribution of cells (pores) and resulting cell-size variations. This disorder contrasts with engineered, structural cellular solids, such as hexagonal honeycombs and micro-truss materials, which are typically highly ordered. Since nature is clearly capable of complex material design, we suggest that highly ordered structure should be readily encountered in biological cellular materials if that order was advantageous. Instead, we hypothesize that structural disorder in cellular solids may itself provide certain benefits in mechanical performance, principally as a toughening mechanism.

Certainly, biological materials display a rich domain of design strategies for optimizing mechanical performance, e.g.: 1) the layering of bending-dominated and stretching-dominated microstructures, 2) weak interfaces, 3) functionally gradient materials, and 4) crack bridging by fibrous elements (7, 10-17). For example, to limit catastrophic failure the hierarchical organic/inorganic structures within bone and nacre significantly increase the flaw tolerance and effective work of fracture compared to engineered ceramics (13-15, 18, 19).

Surprisingly, the spatial disorder of biological cellular materials and its role in mechanical performance have not been analyzed or quantified previously. Herein, we have collected cross-sectional images (our own specimens and sourced from literature, **Table S1**) of biological cellular materials across a wide range of species and length scales (**Fig 1a-f**). We use the Voronoi tessellation as a model to both simulate and quantify disorder, as cell size variation (20). Through an image analysis algorithm, we generated representative Voronoi structures for each image using the centroids of the open cells as nucleation sites (details available in Supplementary Materials, SM). The regular hexagonal honeycomb (RHH) is considered as a special case of Voronoi tessellation where all nucleation sites are hexagonally close-packed and even spacing, r_{hex} . For general 2D cellular structures, a quantitative ‘disorder parameter’ δ can be defined using the minimum distance between centroid spacings ‘ s ’ as (20):

$$\delta = \frac{s}{r_{hex}} \quad (1)$$

Examples of resulting Voronoi structures with δ from 0.1 to 1.0, and the corresponding cell size distributions are shown in **Fig. 1g**.

Remarkably, the biological materials, from trabecular bone to plant stems and fungi, generally fall into well-defined ranges of disorder (**Fig. 1i**), e.g.; woods and fungi from $\delta = 0.6$ to 0.8; trabecular bone and dentin from $\delta = 0.55$ to 0.65. Those biological materials associated with organisms constructing housing (corals, bee honeycomb) have relatively high order ($\delta = 0.9$ to

0.97). We also find that common engineering metal and polymer foams, with structures dependent on surface tension effects (21, 22), are generally much more disordered ($\delta = 0.2$ to 0.5). Regular hexagonal structural honeycombs (lightweight sandwich panels) have $\delta = 1.0$. These results suggest there may be a certain *optimal* degree of disorder, which we refer to as ‘pseudo-order’, in biogenic cellular materials. The analysis in **Fig. 1i** is not intended to be exhaustive, but to highlight several representative materials and tissues from organisms spanning four Eukaryotic kingdoms.

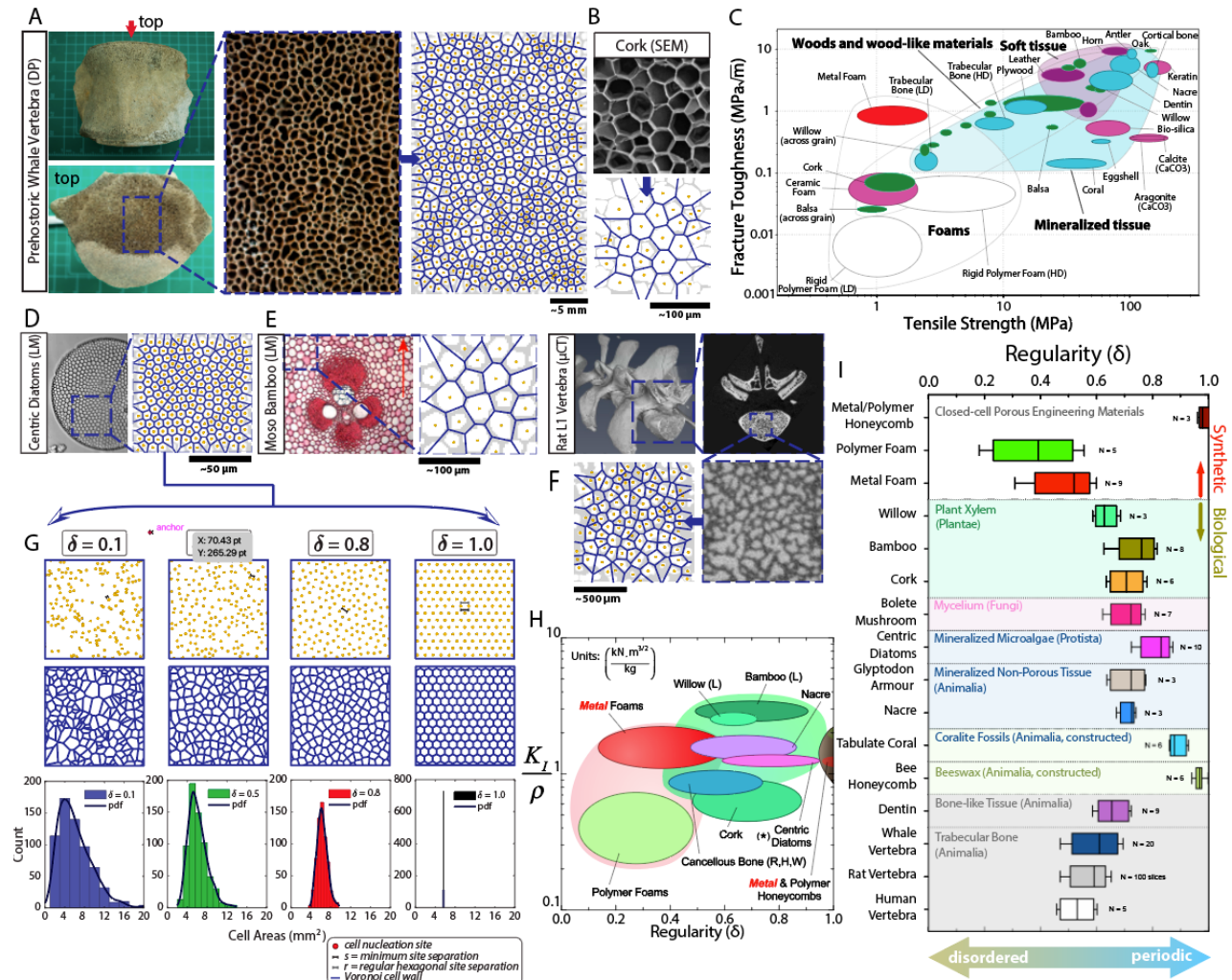


Fig. 1: Examples of biomaterials with disordered in-plane pore distributions and their superimposed Voronoi tessellations: (A) axial trabecular bone in whale vertebra; (B) radial cross-section of cork cell walls; (D) surface features in silica diatom frustule (*Coscinodiscus radiatus*); (E) cross-section of parenchyma cells in Moso bamboo; (F) axial trabecular bone in rat vertebra. Images (B), (D) and (E) adapted from Refs. (24-26), respectively. (G) Geometric effects of increasing regularity (δ) on Voronoi nucleation site distribution, cell morphology, and cell area distribution. (C) Material property map for fracture toughness and tensile strength in natural and foamed materials. Values sourced from CES EduPack (2013). (H) New material property chart for density-normalized fracture toughness demonstrating relationship with newly measured δ values. (I) δ values measured by image analysis for all surveyed cellular materials (sample details in SM). N describes number of images analyzed.

To compare the mechanical behaviour of these architectures, **Fig. 1c** presents the material property space for fracture toughness and tensile strength in biogenic and engineered cellular solids (23). The 'best' performance (high strength *and* damage tolerance) exists at the upper right-hand corner. It is clear that biogenic materials generally outperform engineered cellular solids, despite being composed of brittle constituents, such as calcium carbonate, apatites, silica, and cellulose. If we compare the normalized fracture toughness data from **Fig. 1c** for a range of common biological structural materials as a function of the disorder (δ) (**Fig. 1h**), the highest specific toughness values are found for materials with the 'pseudo-ordered' δ values (0.6 to 0.8) found previously.

To date, there are no studies on the role that disorder plays in flaw tolerance or mechanical fracture of biogenic cellular materials, and few studies on the role of disorder in the mechanical properties of cellular materials generally. Zhu et al. and Sotomayor et al. used finite element (FE) modelling to simulate compressive elastic modulus in 2D honeycombs as a function of increasing disorder (27, 28). The primary failure mechanism of RHH in compression is either sequential plastic collapse of cell walls, or fracture and crushing of brittle cell walls, along close-packed directions, depending on the ductility of the parent material (29, 30). Studies show that point defects (filled cells or cut walls) can disrupt the sequential plastic collapse of cells, to increase damage delocalization in compression (31-33). FE models of impact compression have shown that increased cell irregularity in 2D honeycombs can increase the plateau stress, thereby improving the energy absorption capacity (34-37). There have been no studies that examine the role of disorder in tensile failure of cellular materials, though mode I tensile loading and fracture are common for biological structural materials.

In this work, we examine what role structural disorder contributes to toughening, particularly in tensile loading and fracture conditions, and whether the disorder (pseudo-order) of biogenic cellular materials may provide evolutionary advantage in tissue repair and organism survival. We have taken advantage of digital design and fabrication to generate 2.5D cellular models with systematically increasing degrees of disorder (δ), for the same relative density and material composition.

Results

We have used high-resolution, multi-jet 3D printing to generate 2.5D honeycombs based on varying values of δ . Modern digital fabrication tools provide the opportunity to systematically control disorder. Through uniaxial mechanical testing we compare the properties of disordered honeycombs (DH) with regularity from $\delta=0.1$ to 0.9, with the regular hexagonal honeycomb (RHH), $\delta=1.0$. All throughout, relative density ($\bar{\rho} = 25\%$) and the number of nucleation sites (cells) are kept constant ($n = 314$). A CAD algorithm was built in Grasshopper (Rhinoceros 3D, USA) to convert base coordinates for each tessellation into a 3D solid (**Fig. 2a-d**), similar to the parametric approach of Frølich et al. for non-periodic tessellations in nacre (38). A series of finite element (FE) simulations was also employed to compare and expand on the mechanical performance of the disordered honeycombs. Further details on Voronoi regularity parameter definition and the FE modelling approach used to define fracture toughness are found in SM. Representative tensile stress-strain results are shown in **Fig. 2e**. The peak strength of RHHs ($\delta=1.0$) is higher than all DHs tested, yet also fracture in a single catastrophic event. In contrast,

DHs with $0.1 \leq \delta \leq 0.8$ fail in multiple steps by successive, non-catastrophic fracture with significant variations in crack direction. Each change of direction in the DH's path corresponds to a crack arresting event, visible as small dips in the stress-strain curve (**Movie M1** in SM), with the integrated area underneath the curve (shaded) indicating the total strain energy absorbed. While disordered honeycombs exhibit fracture events before regular honeycombs, their path to final fracture is prolonged, often producing higher energy absorption measurements than regular structures.

The relative effect of disorder on standard tensile properties can be seen by normalizing the DH values to those of the ordered RHH control (**Fig. 3**). The elastic modulus, E , remains largely unaffected by the changes in δ with the mean staying within 5% of the RHH value (**Fig. 3b**). The normalized tensile strength of the RHHs, however, are over 30% stronger than the most disordered $\delta=0.1$ DHs. Interestingly, there is no statistical difference in σ_{max} between the RHH and the $\delta=0.8$; $\delta=0.7$; and $\delta=0.6$ DHs. This may be related to the fact that a near-uniform cell size is approached as $\delta \rightarrow 1.0$ (**Fig. S12, S13**) (32). The effect of disorder is even larger for the energy absorption capacity, with the similar effect that U_v values for $\delta=0.8$; $\delta=0.7$; $\delta=0.6$ are comparable to RHH values. These results show the 'pseudo-ordered' honeycombs of disorder $0.6 \leq \delta \leq 0.8$ exhibit comparable strength and energy absorption values as the regular honeycombs, but also multi-stage failure.

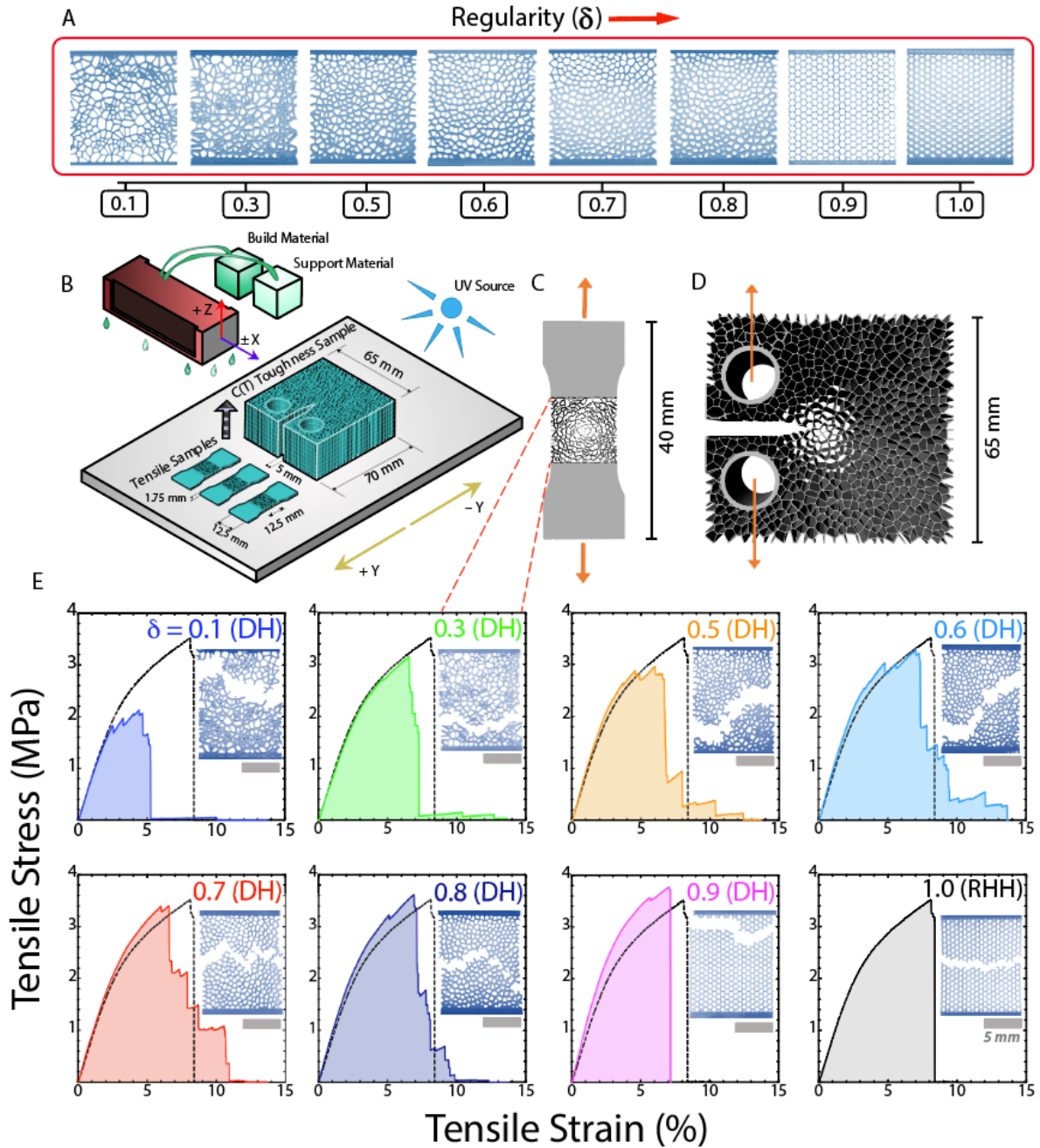


Fig. 2: (A) Photographs of printed dogbone gauge sections in tensile test coupons; (B) Schematic of printing process for (C) dogbone and (D) compact tension geometries. (E) Tensile stress-strain curves showing failure sequence in representative DH and RHH samples with insets showing photographs of the gauge section after fracture. Dotted lines show direct comparisons with the RHH.

Catastrophic fracture features an irrecoverable drop in load bearing capacity. The standard tensile properties in **Fig. 3b-d** are insufficient for describing the effect of disorder on fracture ‘survivability’ as a measure of damage tolerance, or non-catastrophic failure. Hence, three new ‘survivability’ metrics are defined in **Fig. 3a**: tensile strength, instantaneous strain, and energy absorption are measured at the first fracture event (subscript “1”) and compared with the

point of catastrophic failure (subscript “2”, or “max” in the case of peak strength) in **Fig. 3e-g**. Their difference is plotted in **Fig. 3h-j**. We observe increased damage survivability in all properties relative to the RHH for $0.5 \leq \delta \leq 0.8$ DHs, with a remarkable 84% higher mean change in absorbed energy for $\delta=0.8$ (**Fig. 3j**). In other words, pseudo-ordered architectures not only match RHH strength, but they exceed its post-yield damage tolerance (i.e. survivability).

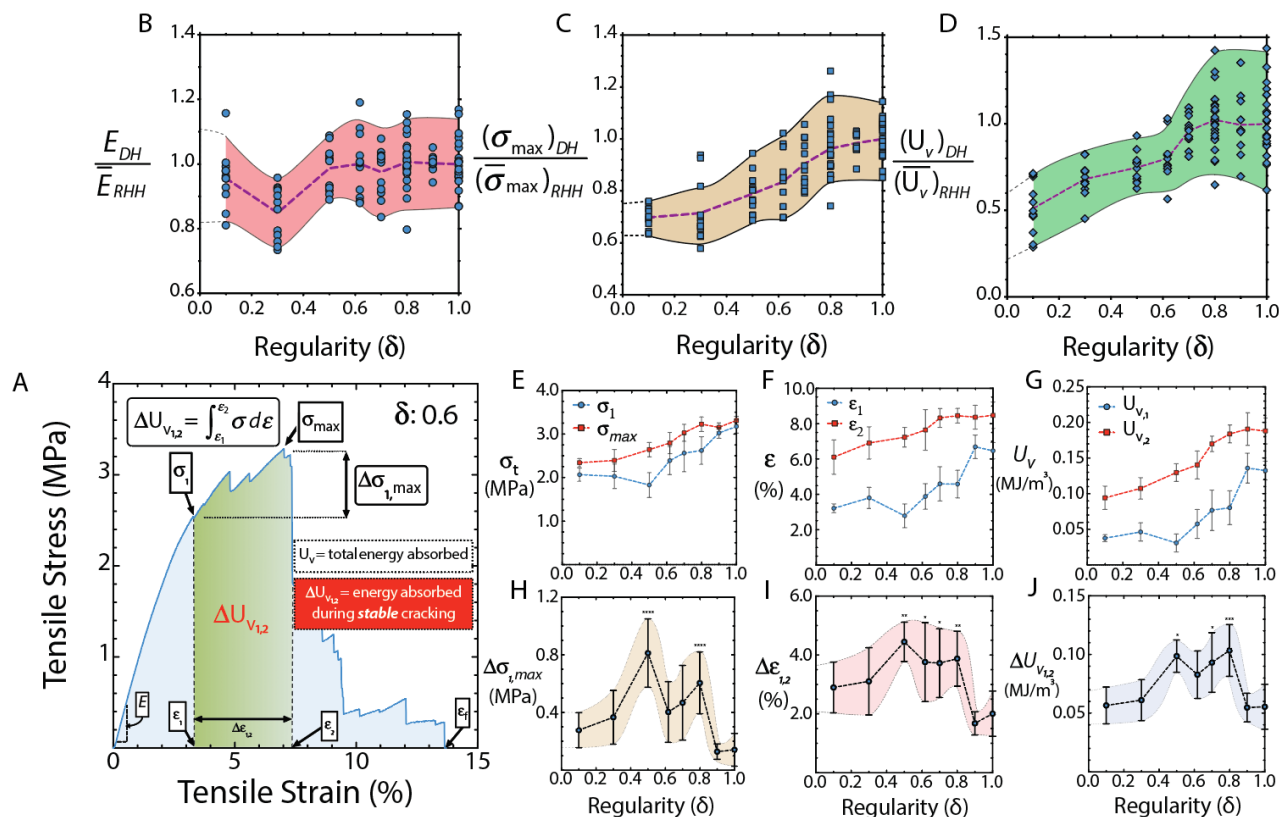


Fig. 3: Summary of uniaxial tensile properties in printed dogbone coupons. (A) Representative stress-strain response for $\delta = 0.6$ illustrates critical measurement locations (subscripts 1, 2 and max) for relevant properties. Change in energy absorption, U_v , during strain-hardening is shown as a shaded green area under the curve. Evolution with δ of normalized (B) Young's modulus; (C) tensile strength; and (D) energy absorption, respectively, plotted from individual tests ($N=12$ samples per δ value, with $N = 24$ for $\delta = 0.8$ and $\delta = 1.0$). Data is normalized against respective mean value from RHH tests. Growth in strength, ductility and energy absorption at critical points is shown in (E), (F), (G), respectively. Divergence between blue and red lines reveals strain-hardening survivability metrics depicted by differentials (δ) in (H), (I), and (J). Error bars indicate standard deviation, while shaded regions are intended to guide the eye.

To gain further insight into the crack propagation mechanics we look to a more robust framework to quantify damage tolerance (15, 39-44). We employ elastic-plastic fracture mechanics (EPFM) on the larger uniaxial coupons outlined in **Fig. 2c** to capture incremental toughness changes during failure via the J -integral compliance method. By tracking tensile force and crack opening displacement (COD), crack paths can be calculated and compared to video-

tracked crack lengths (**Fig. S16**). Here, J is the energy release rate as the work done per unit area of crack advance (45).

The stress-intensity based evolution of fracture toughness, K_J , is plotted against relative crack extension in **Fig. 4a**. Derived from the J -integral, resistance curves of representative honeycombs are shown in the figure for each δ . Details of this derivation and fitting are presented in the SM sections A.5.2 and A.6. The quantity $\Delta a/b_0$ reflects the relative crack growth as it moves through the uncracked portion of material (initial dimension b_0). As such, the test was uniformized with data only considered up to 50% crack propagation (i.e. when $\Delta a/b_0 = 0.5$).

The fracture toughness is clearly influenced by the degree of disorder. In all tests, the honeycomb materials show toughening with crack extension, visualized by the modestly rising resistance curves in **Fig. 4a** (non-zero slope). We observe that DHs with $\delta > 0.3$ have a higher slope than the reference RHH in the initial crack initiation region (up to $\Delta a/b_0 \approx 0.05$), whereas the RHH has a higher slope later in the curve. This is supported by the RHH fracture peak behaviour seen in the force-displacement curve of **Fig. S14**, where load drops were highly regular but of low magnitude and thus corresponded to individual ligament rupture. The fracture toughness values of pseudo-ordered DHs ($\delta \geq 0.6$) and RHHs converge when $\Delta a/b_0 > 0.3$, indicating that disorder has a diminished effect on compliance after some critical crack size. The most significant difference in fracture resistance is thus observed in the crack initiation stage.

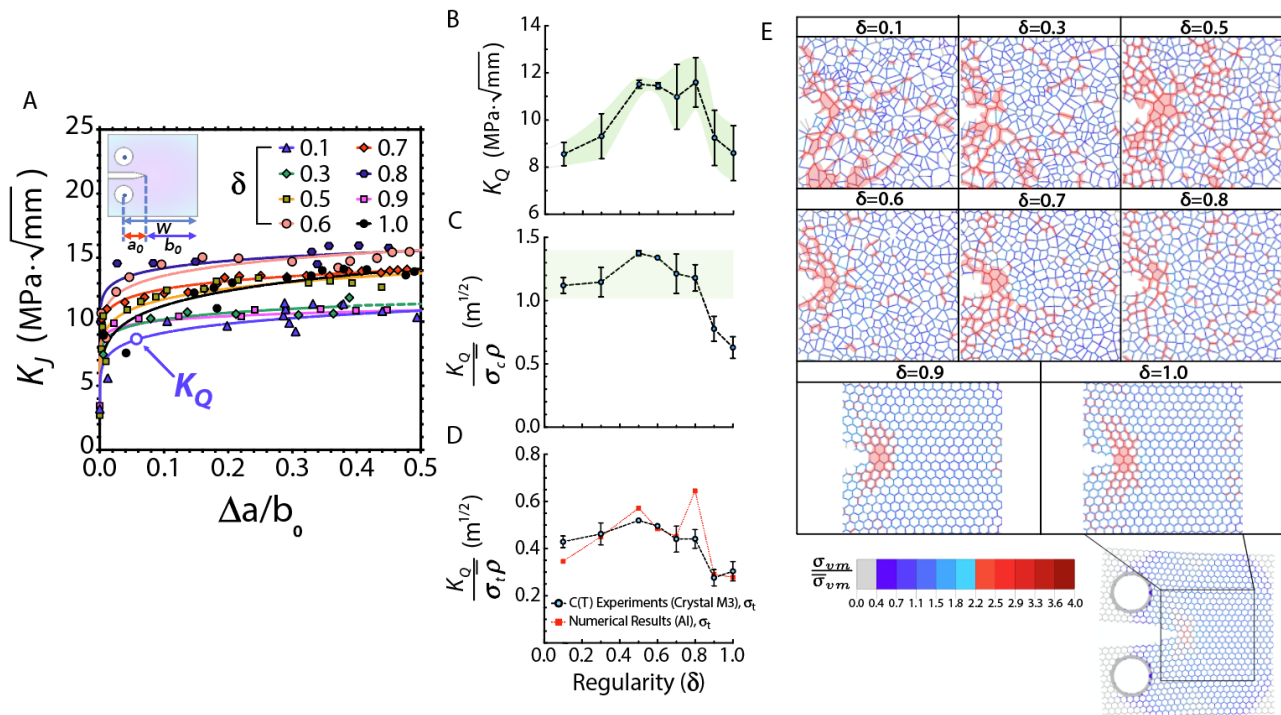


Fig. 4: Experimental and numerical C(T) results showing (A) the response of fracture toughness, K_J , against crack growth Δa , normalized by the initial un-notched sample width, b_0 . Lines through data follow a conventional power law fit. (B) The effects of honeycomb disorder on mode I crack initiation toughness K_Q . Error bars represent standard deviation. Normalization yields (C) the compressive toughness efficiency, and (D) a comparison of numerical and experimental tensile fracture toughness

efficiency. (E) Normalized von mises stress contour maps from FEA taken in the timestep immediately before the first ligament fracture. Legend is normalized by the mean von mises stress summed from all beams in the sample. High-damage zones (continuously high σ_{vm}) are shaded red for visibility. FE simulations are all based on 2D 4-node CPE4R elements.

As with the tensile U_v before, δ is shown to have a significant effect on honeycomb crack initiation toughness (mode I). This is denoted by parameter K_Q , plotted in **Fig. 4b** in lieu of the K_{Ic} seen in bulk solids (See SM section A.6 for derivation). K_Q values of pseudo-hexagonal DHs in the range $0.5 \leq \delta \leq 0.8$ consistently surpass that of regular honeycombs by 28-36%. Mean values of K_Q are reported in Table S4, showing that $\delta = 0.8$ reaches a fracture toughness of $0.37 \text{ MPa}\cdot\text{m}^{1/2}$. Further normalization by mean compressive strength and relative density yields a mode I “toughness efficiency”, $K_Q/(\sigma_c \bar{\rho})$. **Fig. 4c** demonstrates how the efficiency parameter for all DHs is superior to that of the RHH.

Fracture toughness findings were cross-examined by a newly developed finite element (FE) model (method and rationale in SM). **Figs. 4d,e** display numerical results for analogous tests on 2D aluminum honeycombs with identical geometry to the experimental coupons. Remarkably, the toughness efficiency with respect to *tensile* strength ($K_Q/(\sigma_t \bar{\rho})$) exhibits an overlapping trend over experimental data (**Fig. 4d**). **Fig. 4e** compares a side-view of the RHH and DH samples from numerical C(T) tests in the timestep immediately ahead of the first fracture event. It is clear in the superimposed von Mises stress maps that the RHH concentrates stress in the row of cells directly ahead of the crack tip. DHs instead show a much wider dispersion of high stress zones (shaded red for clarity) across the entire sample area, which aligns with previous observations of strain delocalization (28, 46). All together, these behaviours suggest that structural disorder plays an important role in toughening of both brittle and ductile material systems alike.

Discussion

This work demonstrates for the first time, through experiment and simulation, that spatial disorder in cellular solids itself can have dramatic effects on fracture behaviour compared to ordered, regular hexagonal honeycombs (RHH). Disorder helps to delocalize the stress at cracks, inhibits catastrophic crack propagation through path deflection (and multiple cracks), and thus increases effective fracture toughness. As shown experimentally (**Fig. 2e**) and numerically (**Fig. S21**), the fracture paths in the RHHs follow the predominantly straight trajectories of catastrophic fracture. In RHHs, the stress field in any cell ahead of an advancing crack tip is identical. Similarly, in compression, RHHs are known to fail through a propagating cascade of collapse (31). In contrast, the DH cells cause the crack tip path to deflect under influence of unique asymmetric stress fields that emerge after each ligament fracture (**Fig. 4g**). As such, each tip redirection is a pause in crack propagation, promoting DH stability. The most significant path deflections were universally seen in the $0.6 \leq \delta \leq 0.8$ range, while straight-line “fast fracture” sections of crack growth only occur when $\delta < 0.5$ and $\delta \geq 0.9$ (**Fig. 2e**).

The measured toughness and tensile strength values demonstrate how disordered tessellations in the range of $0.6 \leq \delta \leq 0.8$ can match the strength of ordered RHHs while increasing the work of fracture, and ‘survivability’ through crack deflection. The disorder range

around $\delta=0.8$ in particular shows a mode I fracture toughness K_Q that is 36% higher than $\delta=1.0$ (for RHHs). For the first time, these results show that for all other parameters equal (average cell size, area fraction and relative density) there are real mechanical advantages to disorder.

Time-correlated video stills (**Fig. S17**) reveal how toughness enhancements appear to stem from crack tip blunting and deflection mechanisms analogous to those found in biological composites like wood, nacre and bone (10, 11, 16, 17). We adopt Kruzic et al.'s formalism for intrinsic and extrinsic toughening mechanisms (16). Plastic wall bending and “crack diffusion” (sudden fracture bursts) (**Fig. S17b,c**) are deemed as intrinsic events, affecting crack motion ahead of the tip to resist further damage. Small, progressive fracture bursts allow the structure to retain load carrying capacity during failure. Secondly, crack tip bridging is an extrinsic mechanism. Ligament bridges help to further stabilize crack growth in the bulk by effectively holding together splitting regions of the honeycomb. In other words, for $\delta \leq 0.8$ there is a flaw tolerance, in the form of ‘reserve’ structural loading capacity despite the onset of damage. Indeed, Pro and Barthelat recently summarized the universal importance of weak interfaces in the toughness of biological materials (15). We suggest that ‘weak’, sacrificial cell walls in our DHs provide energetically preferred cracking planes, to lead the crack tip away from a single catastrophic path.

Toughening mechanisms and flaw tolerance in biological cellular materials, such as trabecular bone and dentin, have important consequences for tissue repair, and survival. After trauma, it is critical for animals to avoid catastrophic bone fracture for any chance to survive. **Fig. 5** depicts hypothetical stages of fracture in the femoral trochanter of mammalian long bone, together with a typical tensile stress-strain curve for $\delta=0.8$ DH. Fracture events are coupled to a series of stress drops. As such, fracture #1 shows a near-imperceptible loss of loading capacity and quick recovery of plasticity. This could relate to internal micro-cracks within trabecular bone (panel 1, and Fazzalari et al. (47)). Panels 2 – 4 depict partial “greenstick” fractures, whereas 5 shows a severed bone. The containment of fracture partway through the bone cross-section may be seen as an evolutionary design goal, prolonging an injured animal's ability to bear weight on the injury. Such flaw size control has been attributed to crack bridging mechanisms (10, 15, 17, 48, 49), and, recently, trabecular surface plasticity (19). Toughening mechanisms for crack deflection and damage delocalization result in more, smaller cracks, instead of a single, catastrophic crack and large crack opening displacement (COD).

Tissue repair mechanisms are scale dependent and have an *absolute* size limit for defects to be repaired. For example, in bone the ‘primary healing’ mechanism is through the Basic Multicellular Units (BMUs) of osteoclasts and osteoblasts (10, 18, 19, 49) to tunnel through and repair damage by bone degradation and re-deposition. The BMUs can bridge cracks, but only for COD of less than 100-200 μm (**Fig. 5c**) (49). Micro-damage in bone (COD < 100 μm) is common, easily repaired, and part of normal bone remodelling. However, a large COD requires the secondary healing mechanism, requiring much more time (and callus formation). The damage delocalization in disordered honeycombs limits absolute crack size, and thereby also keeps the associated COD gap below a threshold size in bone to enable the primary repair mechanism, and better chance of survival.

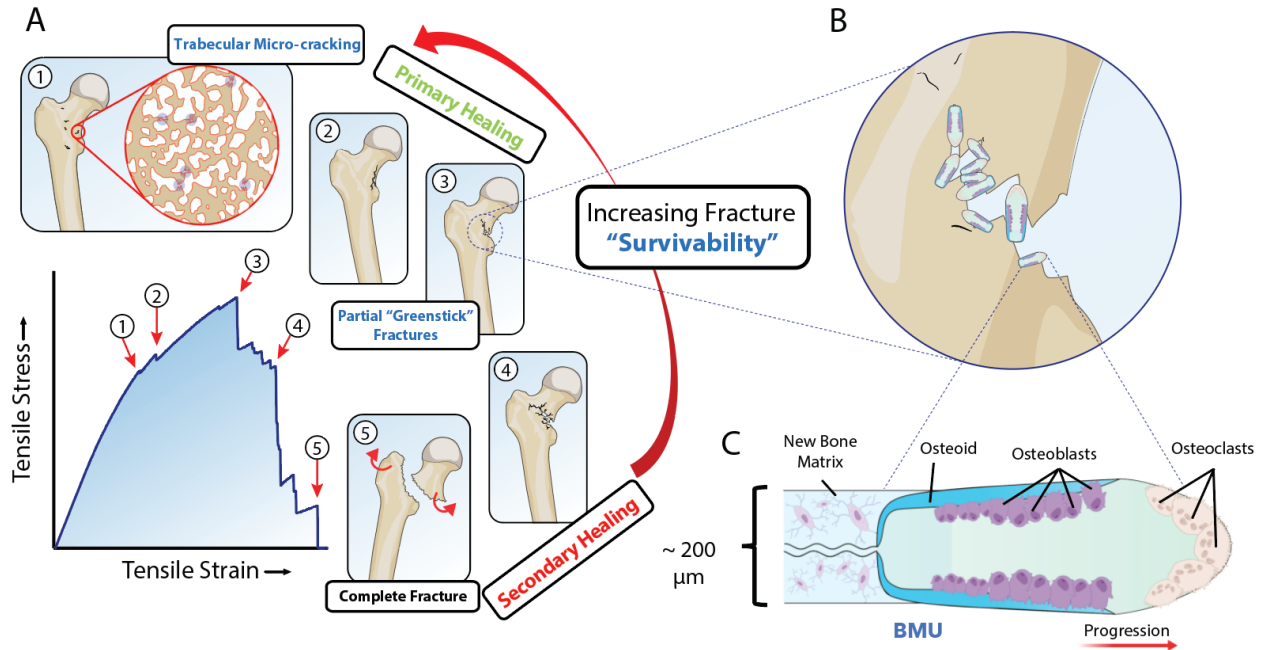


Fig. 5: A) Schematic illustrations of fracture events with increasing severity in a femoral bone, compared to fractures in the stress-strain curve of a $\delta=0.6$ DH. Fractures are categorized by ‘ease’ of reparability by (B) basic multicellular units (BMUs) that can traverse cracks in bone up to a limited scale (100–200 μm), as a mechanism for remodeling and defect repair. (C) Detail illustration depicts the finite structure and scale of the BMU. Distributed, delocalized damage enables effective tissue repair, whereas single, large cracks (large COD) require much more time and biological resources (secondary repair mechanism), and less survivable.

Our study is the first to quantify the disorder in biological cellular materials. We hypothesize that the distinct ranges of pseudo-order we have identified in biological cellular materials for a wide range in organisms is not accidental as it provides mechanical advantage in fracture toughness. In addition to the evolutionary advantage in limiting catastrophic fracture in trauma, we suggest that damage delocalization can enable tissue repair and thereby improve chances of survival. Since we find this similar degree of structural disorder across organisms from the Eukaryotic kingdoms of Animalia, Plantae, Fungi, in our analysis of plant tissue, mammalian bone, sponges and fungi (polypores) (**Fig. 1h,i**), we suggest it is an example of convergent evolution. *In other words, tailored disorder offers an inherent mechanical advantage that is common to all structural cellular solids, and therefore it appears broadly throughout nature.*

Our results suggest that structural cellular materials should not be too highly ordered for optimal mechanical performance. However, there are examples of well-ordered cellular materials in nature. The bee honeycomb and coral examples in **Fig. 1i** are both relatively well-ordered with cells of uniform size. We can speculate that their chief function is to house insect pupa, and polyps, respectively, over mechanical performance. Also, there are many examples of biological cellular materials for structural color, such as in wings of many butterfly species, which require well-defined periodicity for Bragg diffraction. Despite this, certain benefits of disorder in biogenic structural colour materials have also been found. Zollfrank et al. define a “tailored disorder” for optical performance (50), in particular that disordered structures of materials with

deficient refractive index – like chitin – achieves advanced photonic properties. This is shown in the bright isotropic structural colour of the ultra-white beetle which features disordered, pseudo-photonic scales (51).

It seems remarkable that disorder in engineered cellular materials, such as aluminum or polymer foams, has generally been overlooked in structural design. Our work shows the disorder in commercial foams is often much higher than found in biogenic materials. As a result, we suggest that ‘tailored’ structural disorder should be considered as a new design parameter for cellular, architected materials, independent of cell size, connectivity and relative density. Additive manufacturing and digital design techniques for structural optimization (such as topology optimization) allow exploration of a vast new parameter and performance space for architected materials. Recently, engineered hierarchical materials have incorporated toughening mechanisms at the microscale (52-55). We suggest that, as for biological cellular materials, composite design can incorporate ‘designed disorder’ in combination with other toughening mechanisms, such as weak interfaces, crack bridging and gradients.

Conclusions

We have quantified structural disorder in biological cellular materials, and identified limited ranges of disorder which are distinct from those found in typical engineered materials. Spatial disorder in 2D honeycomb significantly increases fracture toughness and flaw tolerance, to limit catastrophic fracture. Disordered honeycombs in the range of $0.6 \leq \delta \leq 0.8$, observed in our biological examples, show elevated fracture toughness and similar strength and stiffness compared to ordered hexagonal controls. The introduction of tailored disorder ($\delta=0.8$) to a 2D honeycomb of identical relative density enables a capacity for strain hardening, damage delocalization and limiting catastrophic failure. Through increased fracture toughness and damage delocalization, we suggest that the pseudo-order of biological cellular materials likely offer evolutionary advantage in survivability, both in limiting fracture and enabling tissue repair. In turn, designed disorder is identified as a potent design tool for future architected materials in engineering applications.

References and Notes:

1. L. J. Gibson, M. F. Ashby, *Cellular solids : structure and properties*. (Cambridge University Press, Cambridge, UK, 1997).
2. L. J. Gibson, M. F. Ashby, B. A. Harley, *Cellular materials in nature and medicine*. (Cambridge University Press, 2010).
3. Y. J. M. Bréchet, in *Materials Design Inspired by Nature: Function Through Inner Architecture*. (The Royal Society of Chemistry, 2013), pp. 1-16.
4. R. O. Ritchie, The conflicts between strength and toughness. *Nature Materials* **10**, 817 (2011).
5. M. F. Ashby, L. Gibson, U. Wegst, R. Olive, The mechanical properties of natural materials. I. Material property charts. *Proc. R. Soc. Lond. A* **450**, 123-140 (1995).
6. U. G. K. Wegst, M. F. Ashby, The mechanical efficiency of natural materials. *Philosophical Magazine* **84**, 2167-2186 (2004).

7. J. Aizenberg *et al.*, Skeleton of Euplectella sp.: structural hierarchy from the nanoscale to the macroscale. *Science* **309**, 275-278 (2005).
8. A. Miserez *et al.*, Effects of laminate architecture on fracture resistance of sponge biosilica: lessons from nature. *Advanced Functional Materials* **18**, 1241-1248 (2008).
9. A. Woesz *et al.*, Micromechanical properties of biological silica in skeletons of deep-sea sponges. *Journal of Materials Research* **21**, 2068-2078 (2006).
10. M. E. Launey, M. J. Buehler, R. O. Ritchie, On the Mechanistic Origins of Toughness in Bone. *Annual Review of Materials Research* **40**, 25-53 (2010).
11. U. G. K. Wegst, H. Bai, E. Saiz, A. P. Tomsia, R. O. Ritchie, Bioinspired structural materials. *Nature Materials* **14**, 23 (2014).
12. M. K. Habibi, Y. Lu, Crack Propagation in Bamboo's Hierarchical Cellular Structure. *Scientific Reports* **4**, 5598 (2014).
13. F. Barthelat, H. Tang, P. D. Zavattieri, C. M. Li, H. D. Espinosa, On the mechanics of mother-of-pearl: A key feature in the material hierarchical structure. *Journal of the Mechanics and Physics of Solids* **55**, 306-337 (2007).
14. A. Khayer Dastjerdi, R. Rabiei, F. Barthelat, The weak interfaces within tough natural composites: Experiments on three types of nacre. *Journal of the Mechanical Behavior of Biomedical Materials* **19**, 50-60 (2013).
15. J. W. Pro, F. Barthelat, The fracture mechanics of biological and bioinspired materials. *MRS Bulletin* **44**, 46-52 (2019).
16. J. J. Kruzic, R. K. Nalla, J. H. Kinney, R. O. Ritchie, Crack blunting, crack bridging and resistance-curve fracture mechanics in dentin: effect of hydration. *Biomaterials* **24**, 5209-5221 (2003).
17. M. E. Launey, P. Y. Chen, J. McKittrick, R. O. Ritchie, Mechanistic aspects of the fracture toughness of elk antler bone. *Acta Biomaterialia* **6**, 1505-1514 (2010).
18. R. Oftadeh, M. Perez-Viloria, J. C. Villa-Camacho, A. Vaziri, A. Nazarian, Biomechanics and Mechanobiology of Trabecular Bone: A Review. *Journal of Biomechanical Engineering* **137**, 0108021-01080215 (2015).
19. A. M. Torres *et al.*, Material heterogeneity in cancellous bone promotes deformation recovery after mechanical failure. *Proceedings of the National Academy of Sciences of the United States of America* **113**, 2892-2897 (2016).
20. H. X. Zhu, S. M. Thorpe, A. H. Windle, The geometrical properties of irregular two-dimensional Voronoi tessellations. *Philosophical Magazine A* **81**, 2765-2783 (2001).
21. M. F. Ashby, The properties of foams and lattices. *Philosophical Transactions of the Royal Society A: Mathematical, Physical and Engineering Sciences* **364**, 15-30 (2006).
22. N. J. Mills, in *Polymer Foams Handbook*, N. J. Mills, Ed. (Butterworth-Heinemann, Oxford, 2007), pp. 39-67.
23. CES EduPack software, Granta Design Limited. (2013).
24. S. P. Silva *et al.*, Cork: properties, capabilities and applications. *International Materials Reviews* **50**, 345-365 (2005).
25. V. de Vos, thesis, Van Hall Larenstein University of Applied Sciences, Wageningen, Netherlands (2010).
26. J. Park *et al.*, Diatom assemblages on Nanaura mudflat, Ariake Sea, Japan: with reference to the biogeography of marine benthic diatoms in Northeast Asia. *Botanical Studies* **53**, (2012).

27. H. X. Zhu, J. R. Hobdell, A. H. Windle, Effects of cell irregularity on the elastic properties of 2D Voronoi honeycombs. *Journal of the Mechanics and Physics of Solids* **49**, 857-870 (2001).
28. O. E. Sotomayor, H. V. Tippur, Role of cell regularity and relative density on elasto-plastic compression response of random honeycombs generated using Voronoi diagrams. *International Journal of Solids and Structures* **51**, 3776-3786 (2014).
29. Y. Sun, Q. M. Li, Dynamic compressive behaviour of cellular materials: A review of phenomenon, mechanism and modelling. *International Journal of Impact Engineering* **112**, 74-115 (2018).
30. D. Mohr, M. Doyoyo, Nucleation and propagation of plastic collapse bands in aluminum honeycomb. *Journal of Applied Physics* **94**, 2262-2270 (2003).
31. O. Prakash, P. Bichebois, Y. Brechet, F. Louchet, J. D. Embury, A note on the deformation behaviour of two-dimensional model cellular structures. *Philosophical Magazine A* **73**, 739-751 (1996).
32. M. J. Silva, L. J. Gibson, The effects of non-periodic microstructure and defects on the compressive strength of two-dimensional cellular solids. *International Journal of Mechanical Sciences* **39**, 549-563 (1997).
33. H. Nakamoto, T. Adachi, W. Araki, In-plane impact behavior of honeycomb structures randomly filled with rigid inclusions. *International Journal of Impact Engineering* **36**, 73-80 (2009).
34. Z. Zheng, J. Yu, J. Li, Dynamic crushing of 2D cellular structures: A finite element study. *International Journal of Impact Engineering* **32**, 650-664 (2005).
35. K. Li, X. L. Gao, J. Wang, Dynamic crushing behavior of honeycomb structures with irregular cell shapes and non-uniform cell wall thickness. *International Journal of Solids and Structures* **44**, 5003-5026 (2007).
36. A. Ajdari, H. Nayeib-Hashemi, A. Vaziri, Dynamic crushing and energy absorption of regular, irregular and functionally graded cellular structures. *International Journal of Solids and Structures* **48**, 506-516 (2011).
37. W. Chen, Z. Liu, H. M. Robinson, J. Schroers, Flaw tolerance vs. performance: A tradeoff in metallic glass cellular structures. *Acta Materialia* **73**, 259-274 (2014).
38. S. Frølich, J. C. Weaver, M. N. Dean, H. Birkedal, Uncovering Nature's Design Strategies through Parametric Modeling, Multi-Material 3D Printing, and Mechanical Testing *Advanced Engineering Materials* **19**, e201600848 (2017).
39. Air Force Research Laboratory, DTD Handbook: Handbook for Damage Tolerant Design. (2009).
40. J. Tomblin, T. Lacy, B. Smith, S. Hooper, A. Vizzini, "Review of damage tolerance for composite sandwich airframe structures," (WICHITA STATE UNIV KS, 1999).
41. N. A. Fleck, X. Qiu, The damage tolerance of elastic-brittle, two-dimensional isotropic lattices. *Journal of the Mechanics and Physics of Solids* **55**, 562-588 (2007).
42. I. Q. Alonso, N. Fleck, Damage tolerance of an elastic-brittle diamond-celled honeycomb. *Scripta Materialia* **56**, 693-696 (2007).
43. N. A. Fleck, V. S. Deshpande, M. F. Ashby, Micro-architected materials: past, present and future. *Proceedings of the Royal Society A: Mathematical, Physical and Engineering Science* **466**, 2495-2516 (2010).

44. O. Kolednik, J. Predan, F. D. Fischer, P. Fratzl, Bioinspired Design Criteria for Damage-Resistant Materials with Periodically Varying Microstructure. *Advanced Functional Materials* **21**, 3634-3641 (2011).
45. ASTM E1820-18, Standard Test Method for Measurement of Fracture Toughness, ASTM International, West Conshohocken, PA, 2018, www.astm.org
46. I. Christodoulou, P. J. Tan, Crack initiation and fracture toughness of random Voronoi honeycombs. *Engineering Fracture Mechanics* **104**, 140-161 (2013).
47. N. L. Fazzalari, M. R. Forwood, K. Smith, B. A. Manthey, P. Herreen, Assessment of Cancellous Bone Quality in Severe Osteoarthritis: Bone Mineral Density, Mechanics, and Microdamage. *Bone* **22**, 381-388 (1998).
48. O. A. Tertuliano, J. R. Greer, The nanocomposite nature of bone drives its strength and damage resistance. *Nature Materials* **15**, 1195 (2016).
49. D. Taylor, J. G. Hazenberg, T. C. Lee, Living with cracks: Damage and repair in human bone. *Nature Materials* **6**, 263 (2007).
50. C. Zollfrank, Bioinspired material surfaces – Science or engineering? *Scripta Materialia* **74**, 3-8 (2014).
51. S. L. Burg *et al.*, Liquid–liquid phase separation morphologies in ultra-white beetle scales and a synthetic equivalent. *Communications Chemistry* **2**, 100 (2019).
52. L. R. Meza, S. Das, J. R. Greer, Strong, lightweight, and recoverable three-dimensional ceramic nanolattices. *Science* **345**, 1322-1326 (2014).
53. L. R. Meza *et al.*, Resilient 3D hierarchical architected metamaterials. *Proceedings of the National Academy of Sciences* **112**, 11502-11507 (2015).
54. X. Zheng *et al.*, Multiscale metallic metamaterials. *Nature materials* **15**, 1100 (2016).
55. J. Bauer *et al.*, Nanolattices: An Emerging Class of Mechanical Metamaterials. *Advanced Materials* **29**, 1701850 (2017).

Supplementary Material References:

56. W. L. Martinez, A. R. Martinez, *Computational statistics handbook with MATLAB*. (Chapman and Hall/CRC, 2007).
57. K. Li, X. L. Gao, G. Subhash, Effects of cell shape and cell wall thickness variations on the elastic properties of two-dimensional cellular solids. *International Journal of Solids and Structures* **42**, 1777-1795 (2005).
58. O. E. Sotomayor, H. V. Tippur, Role of cell regularity and relative density on elastoplastic compression response of 3-D open-cell foam core sandwich structure generated using Voronoi diagrams. *Acta Materialia* **78**, 301-313 (2014).
59. J. Schindelin *et al.*, Fiji: an open-source platform for biological-image analysis. *Nature Methods* **9**, 676 (2012).
60. P. G. Dixon *et al.*, 3D printed structures for modeling the Young's modulus of bamboo parenchyma. *Acta Biomaterialia* **68**, 90-98 (2018).
61. P. G. Dixon *et al.*, Comparison of the flexural behavior of natural and thermo-hydro-mechanically densified Moso bamboo. *European Journal of Wood and Wood Products* **74**, 633-642 (2016).
62. P. Ahvenainen *et al.*, Spatially-localized bench-top X-ray scattering reveals tissue-specific microfibril orientation in Moso bamboo. *Plant Methods* **13**, 5 (2017).

63. R. Ito, H. Miyafuji, N. Kasuya, Rhizome and root anatomy of moso bamboo (*Phyllostachys pubescens*) observed with scanning electron microscopy. *Journal of Wood Science* **61**, 431-437 (2015).
64. L. Gibson, K. Easterling, M. F. Ashby, The structure and mechanics of cork. *Proceedings of the Royal Society of London. A. Mathematical and Physical Sciences* **377**, 99-117 (1981).
65. N. J. B. Brereton *et al.*, X-ray micro-computed tomography in willow reveals tissue patterning of reaction wood and delay in programmed cell death. *BMC Plant Biology* **15**, 83 (2015).
66. N. J. B. Brereton, Sample Preparation for X-ray Micro-computed Tomography of Woody Plant Material and Associated Xylem Visualisation Techniques. *Bio-protocol* **6**, e1767 (2016).
67. J. Rosenkrantz, in *Nervous System Blog*. (<https://n-e-r-v-o-u-s.com/blog/?p=6055>, 2014), vol. 2021.
68. L. J., in *Lauren J. Writes*. (<https://laurenjwrites.com/home/2019/11/22/mushroom-foraging>), vol. 2021.
69. A. Rockefeller. (Mushroom Observer, https://mushroomobserver.org/127881?user_locale=en, 2013), vol. 2021.
70. N. Yao, A. K. Epstein, W. W. Liu, F. Sauer, N. Yang, Organic–inorganic interfaces and spiral growth in nacre. *Journal of the Royal Society Interface* **6**, 367-376 (2008).
71. N. Sun *et al.*, Morphometrics and palaeoecology of the coral *Agetolites* from the Xiazhen Formation (Upper Ordovician), Zhuzhai, South China. *Alcheringa: An Australasian Journal of Palaeontology* **40**, 251-274 (2016).
72. D.-C. Lee *et al.*, Revised stratigraphy of the Xiazhen Formation (Upper Ordovician) at Zhuzhai, South China, based on palaeontological and lithological data. *Alcheringa: An Australasian Journal of Palaeontology* **36**, 387-404 (2012).
73. J. Stel, C. M., The Silurian Upper Burgsvik and Lower Hamra-Sundre Beds, Gotland. *Scripta Geol* **44**, (1977).
74. E. Soibelzon, Los Mamíferos del Ensenadense (Pleistoceno Inferior-Medio) del Este de la Región Pampeana, con énfasis en los Xenarthra. *Bioestratigrafía, diversidad y correlaciones biogeográficas*, (2008).
75. F. Cuadrelli *et al.*, Late Pleistocene Glyptodontinae (Mammalia, Xenarthra, Glyptodontidae) from southern South America: a comprehensive review. *Journal of Vertebrate Paleontology* **38**, e1525390 (2018).
76. J. Rosenkrantz, in *Nervous System Blog*. (<https://n-e-r-v-o-u-s.com/blog/?p=2242>, 2012), vol. 2021.
77. M. S. Hale, J. G. Mitchell, Functional morphology of diatom frustule microstructures: hydrodynamic control of Brownian particle diffusion and advection. *Aquatic Microbial Ecology* **24**, 287-295 (2001).
78. B. Tesson, M. Hildebrand, Extensive and Intimate Association of the Cytoskeleton with Forming Silica in Diatoms: Control over Patterning on the Meso- and Micro-Scale. *PLOS ONE* **5**, e14300 (2010).
79. J. Piper, A review of high-grade imaging of diatoms and radiolarians in light microscopy optical- and software-based techniques. *Diatom Research* **26**, 57-72 (2011).

80. F. Hilaluddin, C.-P. Leaw, P.-T. Lim, Fine structure of the diatoms *Thalassiosira* and *Coscinodiscus* (Bacillariophyceae): Light and electron microscopy observation. *Annals of Microscopy* **10**, 28-35 (2010).
81. M. E. Meave del Castillo, M. E. Zamudio-Resendiz, L. F. Fernandes, *Fryxelliella sepulvedana* sp. nov. (Triceratiaceae, Bacillariophyta), uma rara espécie do Pacífico Mexicano. *Iheringia Série Botânica* **63**, 177-185 (2008).
82. P. A. Sims, THE GENUS *PRAETRICERATIUM* GEN. NOV.: A SURVEY OF EUPODISCOID GENERA WITH A SIPHO MARGINALIS. *Diatom Research* **16**, 399-416 (2001).
83. Päusele, in *Le Naturaliste Forum*. (<http://www.lenaturaliste.net/forum/viewtopic.php?f=292&t=12151#p66982>, 2013), vol. 2018.
84. F. Nazzi, The hexagonal shape of the honeycomb cells depends on the construction behavior of bees. *Scientific Reports* **6**, 28341 (2016).
85. F. H. Kaatz, A. Bultheel, T. Egami, Order parameters from image analysis: a honeycomb example. *Naturwissenschaften* **95**, 1033 (2008).
86. A. Hailu, K. Biratu, Determination of Bee Space and Cell Dimensions for Jimma Zone Honeybee Eco-Races (*Apis malifera*), Southwest Ethiopian. *Journal of Biology, Agriculture and Healthcare* **6**, 41-46 (2016).
87. S. Hines D Fau - Xu *et al.*, Effect of a stannous fluoride toothpaste on dentinal hypersensitivity: In vitro and clinical evaluation.
88. S. Seyedkavoosi, I. Sevostianov, Multiscale micromechanical modeling of the elastic properties of dentin. *Journal of the Mechanical Behavior of Biomedical Materials* **100**, 103397 (2019).
89. C. Montoya, S. Arango-Santander, A. Peláez-Vargas, D. Arola, E. A. Ossa, Effect of aging on the microstructure, hardness and chemical composition of dentin. *Archives of Oral Biology* **60**, 1811-1820 (2015).
90. M. Saadatfar *et al.*, Imaging of metallic foams using X-ray micro-CT. *Colloids and Surfaces A: Physicochemical and Engineering Aspects* **344**, 107-112 (2009).
91. N. Babcsan *et al.*, Characterisation of ALUHAB Aluminium Foams with Micro-CT. *Procedia Materials Science* **4**, 69-74 (2014).
92. C. Körner, Foam formation mechanisms in particle suspensions applied to metal foams. *Materials Science and Engineering: A* **495**, 227-235 (2008).
93. B. M. Patterson, K. Henderson, Z. Smith, Measure of morphological and performance properties in polymeric silicone foams by X-ray tomography. *Journal of Materials Science* **48**, 1986-1996 (2013).
94. M. Nacucchi, F. D. Pascalis, M. Scatto, L. Capodici, R. Albertoni, Structural analysis of advanced polymeric foams by means of high resolution X-ray computed tomography. *AIP Conference Proceedings* **1749**, 020009 (2016).
95. F. De Pascalis, M. Nacucchi, M. Scatto, R. Albertoni, Quantitative characterisation of low-density, high performance polymeric foams using high resolution X-ray computed tomography and laser confocal microscopy. *NDT & E International* **83**, 123-133 (2016).
96. N. P. Daphalapurkar, J. C. Hanan, N. B. Phelps, H. Bale, H. Lu, Tomography and Simulation of Microstructure Evolution of a Closed-Cell Polymer Foam in Compression. *Mechanics of Advanced Materials and Structures* **15**, 594-611 (2008).

97. A. S. M. Ashab, D. Ruan, G. Lu, S. Xu, C. Wen, Experimental investigation of the mechanical behavior of aluminum honeycombs under quasi-static and dynamic indentation. *Materials & Design* **74**, 138-149 (2015).
98. ASTM D638-14, Standard Test Method for Tensile Properties of Plastics, ASTM International, West Conshohocken, PA, 2014, www.astm.org
99. M. O'Masta, L. Dong, L. St-Pierre, H. Wadley, V. Deshpande, The fracture toughness of octet-truss lattices. *Journal of the Mechanics and Physics of Solids* **98**, 271-289 (2017).
100. J. Sumpter, C. Turner, in *Cracks and fracture*. (ASTM International, 1976).
101. H. Ernst, P. Paris, M. Rossow, J. Hutchinson, in *Fracture Mechanics: Proceedings of the Eleventh National Symposium on Fracture Mechanics: Part I*. (ASTM International, 1979).
102. X.-K. Zhu, J. A. Joyce, Review of fracture toughness (G, K, J, CTOD, CTOA) testing and standardization. *Engineering Fracture Mechanics* **85**, 1-46 (2012).
103. ASTM D695-15, Standard Test Method for Compressive Properties of Rigid Plastics, ASTM International, West Conshohocken, PA, 2015, www.astm.org
104. H. Hooputra, H. Gese, H. Dell, H. Werner, A comprehensive failure model for crashworthiness simulation of aluminium extrusions. *International Journal of Crashworthiness* **9**, 449-464 (2004).
105. F. Meng, C. Chen, J. Song, Lattice trapping and crack decohesion in graphene. *Carbon* **116**, 33-39 (2017).
106. J. S. Huang, L. J. Gibson, Fracture toughness of brittle honeycombs. *Acta Metallurgica et Materialia* **39**, 1617-1626 (1991).
107. A. T. Lausic, thesis, University of Toronto, Toronto, ON (2016).
108. V. Q. Truong, thesis, University of Toronto, Toronto, ON (2017).
109. J. Rice, P. Paris, J. Merkle, in *Progress in flaw growth and fracture toughness testing*. (ASTM International, 1973).
110. Z. H. Aitken, S. Luo, S. N. Reynolds, C. Thaulow, J. R. Greer, Microstructure provides insights into evolutionary design and resilience of *Coscinodiscus* sp. frustule. *Proceedings of the National Academy of Sciences* **113**, 2017-2022 (2016).

Acknowledgments: We thank Zachary Fishman and Prof. Cari Whyne of the Sunnybrook Research Institute for their expertise and provision of experimental x-ray μ CT data for vertebral rat specimens. We are indebted to Dr. Dan Grozea for his mechanical testing expertise and gratefully acknowledge Prof. Marc Grynypas for his useful discussions and insights on trabecular bone mechanics.

Funding: This work was supported through the Natural Sciences and Engineering Research Council of Canada (NSERC) Discovery Program #06760 (BDH). D.A.v.E. was supported by the Queen Elizabeth II Graduate Scholarship in Science and Technology.

Competing interests: The authors declare no competing interests.

Data and materials availability: All data is available in the main text or the supplementary materials